




Effects of disorder upon transport and Anderson localization in a finite, two-dimensional Bose gasMojdeh S. Najafabadi ^{*}, Daniel Schumayer , and David A. W. Hutchinson [†]*Dodd-Walls Centre for Photonic and Quantum Technologies, Department of Physics, University of Otago, Dunedin 9016, New Zealand*

(Received 22 September 2021; accepted 26 November 2021; published 13 December 2021)

Anderson localization in a two-dimensional ultracold Bose-gas has been demonstrated experimentally. Atoms were released within a dumbbell-shaped optical trap, where the channel of variable aspect ratio provided the only path for particles to travel between source and drain reservoirs. This channel can be populated with columnar (repulsive) optical potential spikes of square cross section with arbitrary pattern. These spikes constitute impurities, the scattering centers for the otherwise free propagation of the particles. This geometry does not allow for classical potential trapping which can be hard to exclude in other experimental setups. Here we add further theoretical evidence for Anderson localization in this system by comparing the transport processes within a regular and a random pattern of impurities. It is demonstrated that the transport within randomly distributed impurities is suppressed and the corresponding localization length becomes shorter than the channel length. However, if an equal density of impurities are distributed in a regular manner, the transport is only modestly disturbed. This observation corroborates the conclusions of the experimental observation: the localization is indeed attributed to the disorder. Beyond analyzing the density distribution and the localization length, we also calculate a quantum “impedance” exhibiting qualitatively different behavior for regular and random impurity patterns.

DOI: [10.1103/PhysRevA.104.063311](https://doi.org/10.1103/PhysRevA.104.063311)**I. INTRODUCTION**

All real media, however pure, contain disorder which influences their transport properties [1–5]. Indeed, disorder is essential for transport in a regular lattice, for otherwise particles undergo Bloch oscillations [6] and are localized. However, impurities (interstitial atoms, lattice defects, etc.), or even the finite size of the system, which destroy the perfect spatial periodicity, also give rise to residual resistance against electron flow [7]. If the density of impurities is high enough and the typical electron energy is low, the electrons are localized [8–11]; hence, the substance is an insulator. The opposite, the absence of translational symmetry alone, however, does not guarantee an insulating phase [12–15]. The role of disorder in transport can, therefore, be very subtle.

One striking effect of random disorder is the suppression of transport due to destructive interference via multiple propagation paths and the consequent confinement of wave packets. This phenomenon is known as Anderson localization [8,16,17]. This single-particle wave phenomenon does not require any special interaction between particles or specific geometry and so appears ubiquitously in nature and can be present in all kinds of systems [4,18–33]. Since Anderson’s early proposal, the effects of interaction [34,35], dimensionality [16,36], violation of time-reversal symmetry [37], and spin-orbit coupling [38] upon localization have all been analyzed.

Ultracold atomic systems, with their experimental flexibility and precision control of both internal and external

degrees of freedom, make them an excellent platform to explore Anderson localization [39–42]. Localization of atoms has been demonstrated in one dimension (1D) [40,41] and also in 3D [39,42], where, for the latter, the localized and delocalized states were separated by a well-defined mobility edge [43]. However, observation of Anderson localization in two-dimensional ultracold systems has proven to be elusive [44]. Although weak localization in 2D has been reported [45,46], the relatively high percolation threshold [47] of a speckle potential posed serious difficulties and resulted in classical localization. In contrast, in 3D the percolation threshold for speckle disorder is rather small [48], and thus 3D Anderson localization is easily discerned from classical localization. Regarding to 2D, Morong and DeMarco [49] proposed a realistic pointlike disorder potential circumventing the problem of percolation limit. In 2020 White *et al.* [44], after designing a highly flexible optical setup overcoming these technical challenges, demonstrated Anderson localization in a 2D ultracold system.

Here we provide further computational analyses of localization extending this previous work [44]. We consider a 2D dumbbell-shaped trap with potential spikes distributed within the channel. An interacting Bose-Einstein condensate is prepared in its ground state within an initial harmonic trap and centered at the middle of the channel. The harmonic trap is then turned off and the condensate is released within the dumbbell-shaped trap. Although the self-interaction is taken into account in the simulation, mainly to remain close to real-life experiments, its effect is only observable at the very beginning of evolution, when the mean-field energy drives the expansion within the channel. As the density falls rapidly the interaction, together with its influence on the localization, diminishes swiftly.

^{*}shimo048@postgrad.otago.ac.nz[†]david.hutchinson@otago.ac.nz

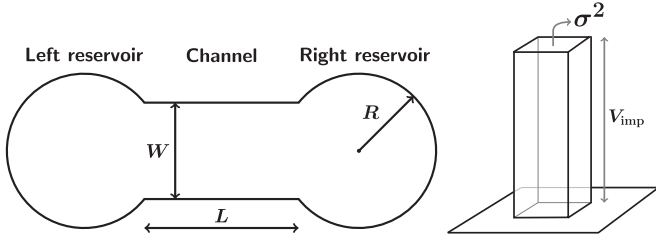


FIG. 1. On the left the schematic of the dumbbell potential is shown: L is the length of the channel, W is the width of the channel, and R is the common radius of the two circular reservoirs. On the right the single columnar potential spike is depicted, showing its square cross section of area σ and height/strength of V_{imp} .

Our main focus is on the transport of particles in two scenarios: impurities distributed randomly or regularly within the channel. We expect these two scenarios to exhibit fundamentally different transport properties. In the analyses we rely on three quantitative measures: the localization length ξ , the momentum distribution k , and an atomtronic impedance, Z , introduced in analogy with that of electrical impedance.

II. DETAILS OF SIMULATIONS

After introducing scales for the energy and for the temporal and spatial coordinates as $\hbar\omega_0$, ω_0^{-1} , $\sqrt{\hbar/m\omega_0}$, respectively, one obtains the numerically more convenient form of the Gross-Pitaevskii equation:

$$i\frac{\partial\psi}{\partial t} = \left[-\frac{1}{2}\nabla^2 + U + \beta|\psi|^2 \right] \psi. \quad (1)$$

The time evolution of the condensate at absolute zero temperature is described by this nonlinear equation adequately. Here U is the dimensionless potential including two terms: the dumbbell trap V_{db} and the overall sum of potential spikes, V_{imp} , representing the impurities. Due to the very nature of this potential term, these impurities are not taken into account as impenetrable hard wall and hence via a Dirichlet boundary condition. Rather these are soft spikes and the wave function can penetrate them as quantum mechanics dictates. As in Ref. [44], the strength of impurities V_{imp} , is constant together with the footprint σ^2 of a single spike (see Fig. 1). The mean-field interaction is measured by $\beta = 2\sqrt{2\pi}Na_s/a_z$, where a_z is the oscillator length corresponding to ω_z , N is the number of ^8Rb atoms, and $a_s = 107a_0$ is the s -wave scattering length. In Eq. (1), ψ is normalized to unity. Parameter values are listed in Table I.

The dumbbell-shaped trap, depicted in Fig. 1, consists of two reservoirs separated by a channel with point scatterers distributed randomly or regularly within the channel. The simulation starts with calculating the ground state of the condensate trapped by the harmonic trap using the imaginary time propagation method [50]. This stationary solution serves as the initial condition for the time evolution, and the condensate is allowed to expand and propagate within the channel, decorated with impurities, towards the reservoirs. Equation (1) is solved numerically by the Runge-Kutta-Fehlberg method [51], and implemented in CUDA language utilizing specialized graphical processor units dedicated for

TABLE I. Symbols and values of parameters.

| Description | | Value |
|---------------------------------|------------------|--------------------------------------|
| Spatial extension (x direction) | L_x | 500 μm |
| Spatial extension (y direction) | L_y | 225 μm |
| Grid points (x direction) | n_x | 1536 |
| Grid points (y direction) | n_y | 768 |
| Reservoir radius | R | 43.2 μm |
| Channel length | L | 180 μm |
| Channel width | W | 36 μm |
| Dumbbell potential depth | V_{db} | 52 nK |
| Impurity height | V_{imp} | 17 nK |
| Impurity cross-section area | σ^2 | 1.4 μm^2 |
| Number of particles | N | 16 000 |
| Frequency of harmonic trap | ω_0 | $2\pi \times 25 \text{ rad s}^{-1}$ |
| Frequency of squeezing trap | ω_z | $2\pi \times 800 \text{ rad s}^{-1}$ |
| Bohr radius | a_0 | $5.29 \times 10^{-11} \text{ m}$ |
| Range of fill-factor | η | [0, 0.3] |

highly parallel tasks. In each simulation, the Gross-Pitaevskii equation evolves for 300 ms, which equates to approximately 20 min of simulation time in the GPU. It is worth mentioning that increasing the fill-factor results in increasing the computational time.

In order to quantify the ‘‘amount’’ of disorder in the channel we introduce a geometric measure, η , based on the overall footprint of the impurities relative to the total available area within the channel:

$$\eta = \frac{A_{\text{imp}}}{A_{\text{channel}}} = n\sigma^2, \quad (2)$$

where n is the density of scatterers and σ^2 is the cross-section area of a single scatterer. For geometrical reasons one may call η the fill-factor. Its meaning is apparent in Fig. 2 where the channel segments of the dumbbell are shown for $\eta = 0.25$ with the impurities distributed randomly [Fig. 2(a)] or regularly [Fig. 2(b)].

We estimate the localization length ξ from fitting the exponential decay on the two- and one-dimensional probability densities, defined as $\rho_{2D} = |\psi|^2$ and

$$\rho_{1D}(x) = \int \rho_{2D}(x, y) dy = \int |\psi(x, y)|^2 dy,$$



FIG. 2. The impurity potential V_{imp} is depicted for randomly (a) and regularly (b) distributed potential spikes for the same fill-factor $\eta = 0.25$. Only the channel segments of the dumbbell trap are shown.

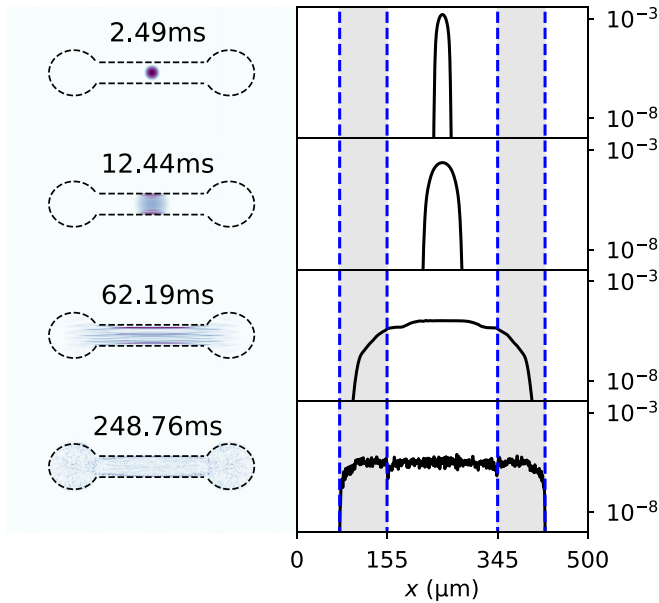


FIG. 3. The left and right columns of graphs show ρ_{2D} and ρ_{1D} , respectively, at different moments in time, covering the entire duration of the simulation. In the right column, ρ_{1D} is plotted on a logarithmic scale, while the left and right reservoirs are depicted as shaded areas. The channel length is $180 \mu\text{m}$. While there is a small portion of the density falling outside of the dumbbell potential, it does not show up in these graphs, as this portion is negligible and thus several orders lower in magnitude than that within the dumbbell.

or in other words, the one-dimensional density is the one-dimensional column density along the x axis, usually easily accessible in an experimental setup.

III. RESULTS

Before we analyze the two main scenarios, let us demonstrate the time evolution of the condensate without potential spikes. This case serves as a benchmark. Figure 3 shows both the one- and the two-dimensional densities as the condensate expands within the channel in the absence of any impurity. It is clear that by $t \simeq 250$ ms the atoms fill the entire dumbbell trap more or less uniformly, exactly what one would expect for a gas trapped in a finite volume. In the following two sections we describe how the spatial distribution of potential spikes alters particle transport.

A. Randomly distributed scatterers

We study the long-time behavior of ρ_{1D} in the channel and in the two reservoirs. For high enough fill-factors we expect localization to occur; hence, the density develops an exponentially decaying profile while expanding within the disordered dumbbell,

$$\rho_{1D}(x) \propto \rho_0 \exp\left(-\frac{2|x|}{\xi}\right), \quad (3)$$

where the origin is at the center of the channel. We call the characteristic parameter the ξ localization length.

Figure 4 shows ρ_{1D} and ρ_{2D} profiles at four moments in time as the condensate expands within the channel with differ-

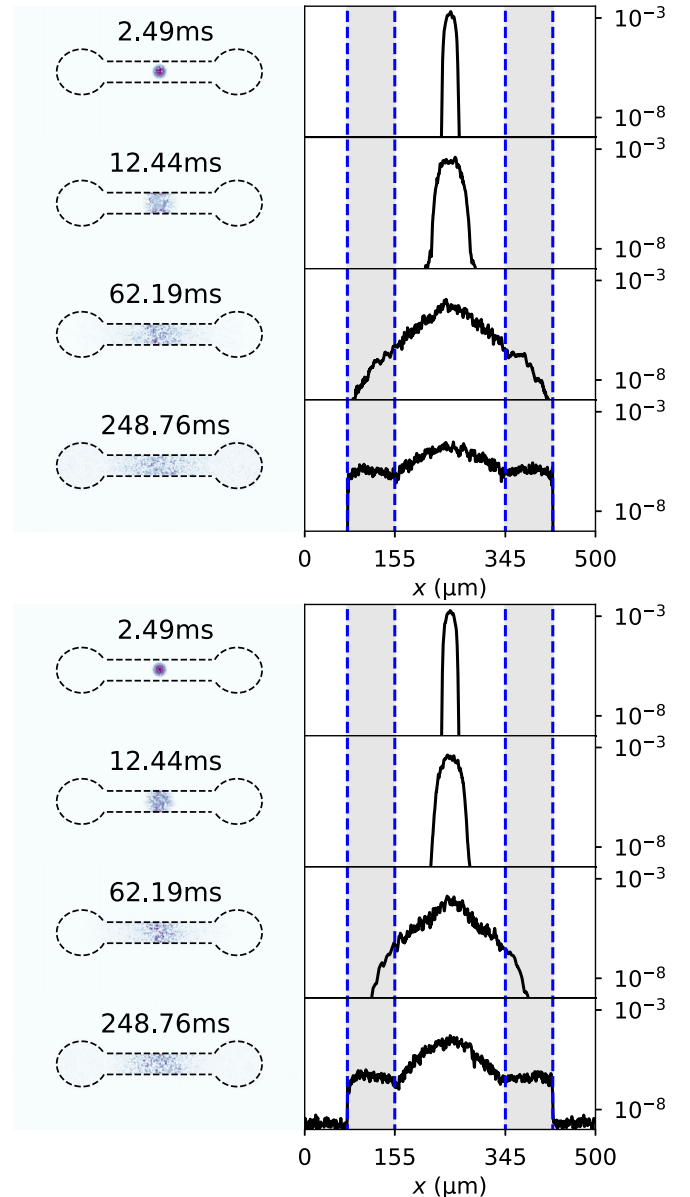


FIG. 4. In the right column the time evolution of ρ_{1D} is depicted for $\eta = 0.05$ (top) and $\eta = 0.2$ (bottom) at $t = 2.49$, 12.44 , and 62.19 and at $t = 248.76$ ms. In the left column ρ_{2D} is shown with the contour of the dumbbell potential overlaid. The geometry is determined by $(L, W, R) = (180, 36, 43) \mu\text{m}$.

ent amount of disorders, $\eta = 0.05$ and 0.2 . For small fill-factor ρ_{1D} does not show any appreciable triangular shape at the center, excluding the possibility of localization. However, for higher disorder, a central peak develops. Towards the end of the time evolution the reservoirs also hold non-negligible amounts of matter. These atoms escape from the disordered channel as their kinetic and mean-field energies are high enough. We substantiate this claim later by calculating the momentum (and hence the energy) distributions of particles in the reservoirs and in the channel. However, increasing η further reduces the density in the reservoirs despite the fact that the strength of individual potential spikes has not changed.

In order to quantify localization Eq. (3) is fitted to ρ_{1D} for $t > 200$ ms treating ξ as fitting parameter. As $\log(\rho_{1D}) \propto |x|$

we defined ξ_{left} and ξ_{right} based on the density for $x < 0$ and $x > 0$. In Fig. 5 some of the curve-fittings are shown for $\eta = 0$ [panel (a)], 0.1 [panel (b)], and 0.2 [panel (c)] together with $\log(\rho_{1D})$ for $t > 200$ ms. The localization lengths ξ_{left} and ξ_{right} and the goodness-of-fit R_{fit}^2 are also provided above each panel [52]. Figure 5(a) shows no exponential decay in either side of the channel; hence, the goodness-of-fit is almost zero. In contrast, ρ_{1D} in Fig. 5(b) starts developing an exponential decay and consequently R_{fit}^2 is elevated to ~ 0.87 . As η increases we expect more particles being localized within the channel due to more interference events, and as a result, ξ decreases: at $\eta = 0.1$ one finds $\xi_{\text{left}}/\xi_{\text{right}} = 95/105 \mu\text{m}$, while $\xi_{\text{left}}/\xi_{\text{right}} = 75/70 \mu\text{m}$ for $\eta = 0.2$. Note, as the impurities are distributed randomly, there is no equality in their number on each side of the channel. Therefore, ξ on two sides of the channel can be slightly different. However, we expect that over numerous configurations at fixed η this difference would vanish.

Figure 6 depicts ξ as a function of η . The localization lengths are calculated by taking an average over the last 50 snapshots of ρ_{1D} . The circular markers represent R_{fit}^2 and show an upward trend as the linear fit becomes better and better for increasing η . More importantly, we also see that ξ falls below the half of the channel length for $\eta > 0.07$.

We may briefly scrutinize the dynamics of localization as well. The localized particles have a fixed localization length unlike for particles in extended states. Figure 7 shows $\xi(t)$ and $R_{\text{fit}}^2(t)$ for four values of η in $[0.02, 0.2]$. For low disorder, the majority of atoms have a large Boltzmann mean free-path; hence, they can escape from the channel, resulting in large $\xi(t)$ and subsequently lower R_{fit}^2 . For higher η we see more stability in the localization length as a function of time. One can argue for a slightly increasing trend after $t = 250$ ms even for the $\eta = 0.2$ case. The point is that, even for $\eta = 0.2$, there are still nonlocalized, high-energy particles which can escape from the channel, reach the wells, and reflect back into the channel again. This process can explain the slightly increasing trend in the last part of $\xi_{\text{left}}(t)$.

In order to catch a localization length less than the system size in a 2D system, we need to consider another important factor, the actual system size, $\sim L$. We consider a dumbbell with a short channel with $\eta = 0.2$. Figure 8 shows ρ_{1D} within different segments of the dumbbells at $t > 200$ ms for $L = 36 \mu\text{m}$. The goodness-of-fit is low while ξ is much larger than L . Moreover, we cannot see any obvious trend in $\xi(\eta)$ or in R_{fit}^2 in Fig. 9. Comparing Figs. 6 and 9, we can safely conclude that in a short channel there are much less scattering events, leading to a larger localization length than the actual system size. Let us to look at the momentum distribution of the atoms. Figure 10 shows $|\mathbf{k}|$ in different segments of the dumbbell, derived through Fourier transform of ρ_{1D} . The momentum distributions of the initial wave packet at $t = 1$ ms are shown in Figs. 10(a), while the momentum distributions in different regions after expansion ($t > 250$ ms) are shown in Figs. 10(b) to 10(d). Figures 10(b) and 10(d) clearly show that for nonzero fill-factor the mean momentum is slightly above $2 \mu\text{m}^{-1}$, indicating that particles with higher momenta escaped from the channel and reached the reservoirs. Atoms with lower momenta are trapped inside of the disordered channel as suggested by Fig. 10(c). In addition, Figs. 10(b) and 10(d) also

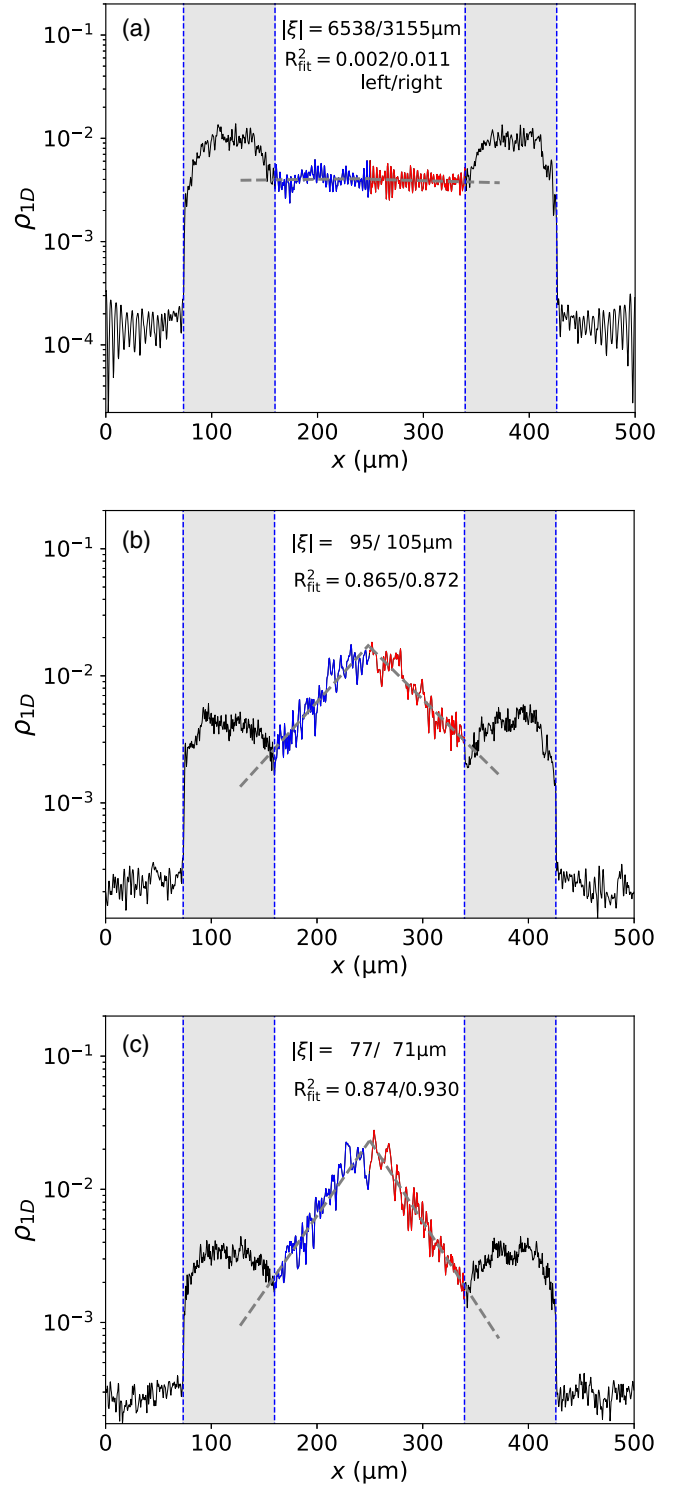


FIG. 5. Figure depicts the one-dimensional density profile over the entire numerical box for $\eta = 0$ (a), 0.1 (b), and 0.2 (c). The vertical dashed lines separate the five important regions: the outermost regions are outside of the dumbbell trap, while the central three regions are the left reservoir, the channel, and the right reservoir. Within the channel the density profile is plotted using two colors for the left and right sides of the channel, respectively. The graph also shows the linear fits to ρ_{1D} . The fitted localization lengths ξ_{left} and ξ_{right} , with the corresponding goodness-of-fit measures, R_{fit}^2 , are given at above the central density.

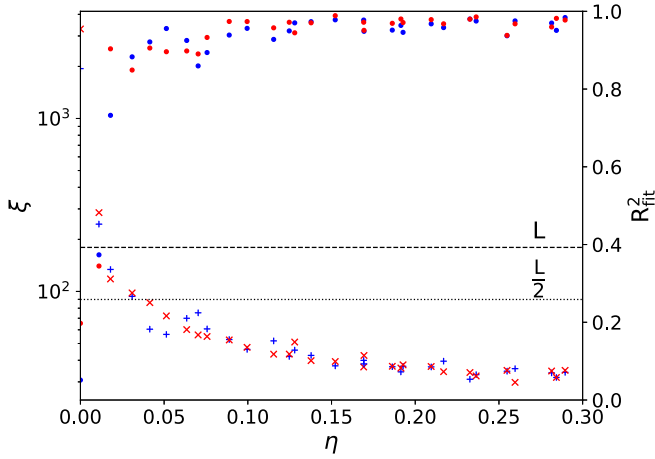


FIG. 6. Localization lengths ξ_{left} and ξ_{right} are depicted as functions of η with blue plus markers (+) and red crosses (x), respectively (left axis). The corresponding measure for goodness-of-fit R_{fit}^2 is also shown with solid circles and applying the same color coding (right axis).

point towards an energy-dependent localization, since even for the highest fill-factor ($\eta = 0.2$) there are particles capable of leaving the channel. This can naively be interpreted as follows: atoms with higher momenta, thus with higher kinetic energy, have shorter wavelengths and are of the order of the mean free-path. The mean free-path can be approximated by the mean spacing between scatterers $\ell_s = \sigma/\sqrt{\eta}$, where σ is the side-length of a single scatterer. The corresponding mean minimal distances for $\eta = 0.1$ and 0.2 are $\ell_s = 4.42 \mu\text{m}$ and $3.1 \mu\text{m}$, respectively. According to Fig. 10(a) the majority of atoms have $|\mathbf{k}| = 1.11 \mu\text{m}^{-1}$, which translates to a wavelength of $\lambda = 2\pi/|\mathbf{k}| = 5.6 \mu\text{m}$, and hence $\sigma < \ell_s < \lambda$. In Figs. 10(b) and 10(d), however, the distributions peak around

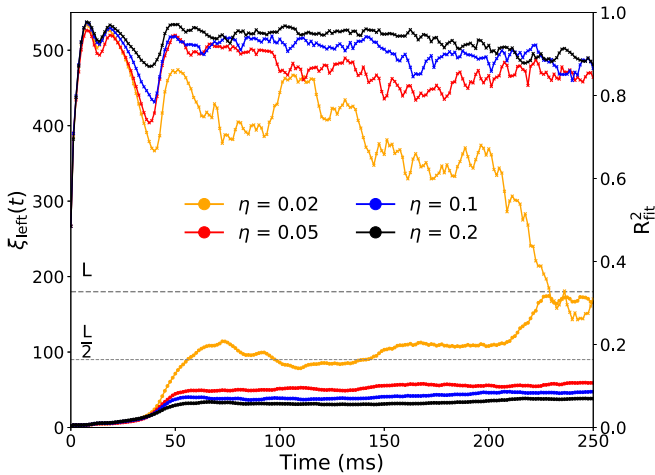


FIG. 7. The apparent localization length ξ_{left} is drawn at each time step for $\eta = 0.02, 0.05, 0.1$, and 0.2 (bottom four curves). The corresponding goodness-of-fit measures are also plotted with matching color (top four curves). The dumbbell geometry is given by $(L, W, R) = (180, 36, 45) \mu\text{m}$. The horizontal gray dashed lines represent the length of the channel, L , and its half, $L/2$, in order to provide comparison.

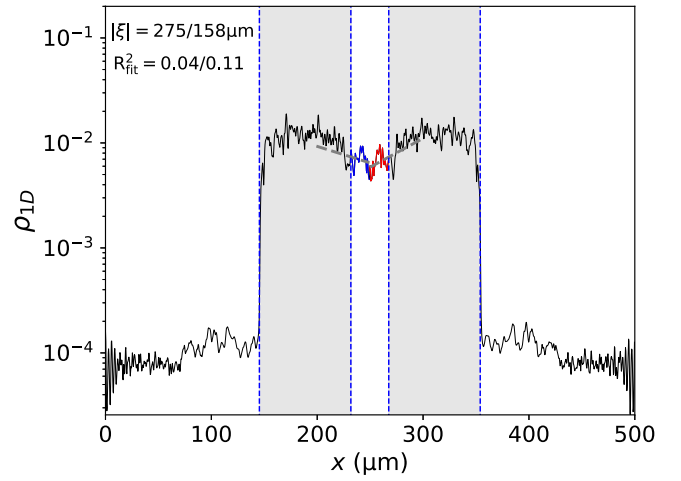


FIG. 8. The one-dimensional density in a short channel is plotted at the end of the time evolution. The left and right reservoirs are indicated with shaded areas and vertical thin blue dashed lines. The thicker dashed lines in the middle of the graph are the linear fits to ρ_{1D} . The dumbbell geometry is $(L, W, R) = (36, 36, 58) \mu\text{m}$.

$2\text{--}3 \mu\text{m}^{-1}$, with corresponding wavelengths being 3.14 to $2 \mu\text{m}$. Therefore, $\sigma < \lambda < \ell_s$. The percolation threshold in this system is ~ 2 nK for $\eta = 0.2$ [49], while the average kinetic energy is ~ 12 nK [cf. Fig 10(a)]; therefore, the setup is below the percolation threshold. In three dimensions the Ioffe-Regel criterion, $|\mathbf{k}|\ell_s \sim 1$, is often quoted as a simple rule, indicating the breakdown of diffusive transport. We remark here that this criterion assumes a well-defined wave vector obtained from a particle's wave packet, and it is not associated with the thermal de Broglie wavelength λ_{dB} . The distribution of wave vectors shown in Figure 10(a) indicates that the Ioffe-Regel criterion will be satisfied by some fraction of the particles, but not necessarily all [see Figs. 10(b) and 10(d)], corroborating our findings that some particles escape into the reservoirs even at $\eta = 0.2$.

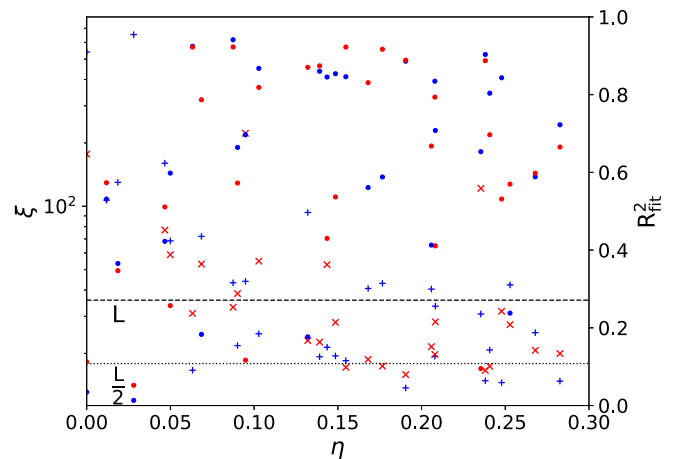


FIG. 9. Localization length ξ as a function of η for a dumbbell with a short channel length of $36 \mu\text{m}$. The symbols and colors are the same as those in Fig. 6.

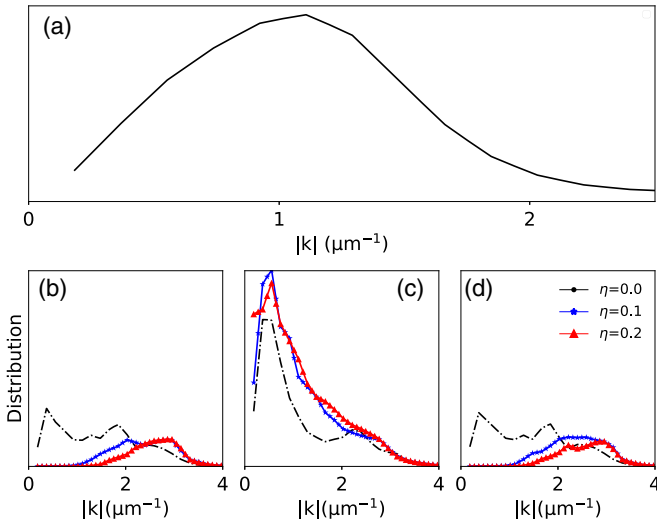


FIG. 10. Momentum distribution of atoms. Panel (a) depicts the initial distribution of the modulus of momentum after releasing the initial harmonic trap ($t = 1$ ms). The distribution of the modulus of momentum is also plotted in the right well (b), in the channel (c), and in the left well (d) after $t > 250$ ms. The curves in panels (b)–(d) correspond to three fill-factors: $\eta = 0.0$ (black dash-dotted line), $\eta = 0.1$ (blue solid line with star-shaped marker), and $\eta = 0.2$ (red solid line with triangle marker). The dumbbell parameters are $(L, W, R) = (180, 36, 45) \mu\text{m}$.

B. Regularly distributed scatterers

We have also analyzed the transport properties of atoms within regularly distributed scatterers and contrasted particle transmission at $t > 250$ ms with that of random scatterers (see Fig. 11). The bottom of Fig. 11 shows ρ_{1D} at $t > 250$ ms. One can clearly see the dumbbell reservoirs being filled up by atoms for regularly distributed scatterers as atoms are in extended states while particles stay localized within the randomly disordered channel. The second obvious difference is in the bottom panels of Fig. 11 where ρ_{1D} exhibits an exponential decay profile for randomly located disorder and no decay for the regularly located potential spikes.

For comparison the particle numbers in the reservoirs (combined) and in the channel are shown as functions of time in Fig. 12. The wells of the dumbbell with regular scatterers are eventually occupied with around twice as many atoms as in the random case. In contrast, the right axis of Fig. 12 shows twice the number of atoms within the channel for the random system compared to that in the periodic case. The normalized atom number in each part is derived by integrating over the density function in each segment along both horizontal and vertical axes and then normalized by the total atom number. One may ask why the atom number in the random case does not become stable with time. The reason lies in the dynamics: some of the atoms, which are in the extended states, reach the walls of the reservoir at longer times. They then reflect back after hitting the reservoir's walls and return into the channel, moving again toward the wells, creating a sloshing background density. This, however, does not affect our general conclusions.

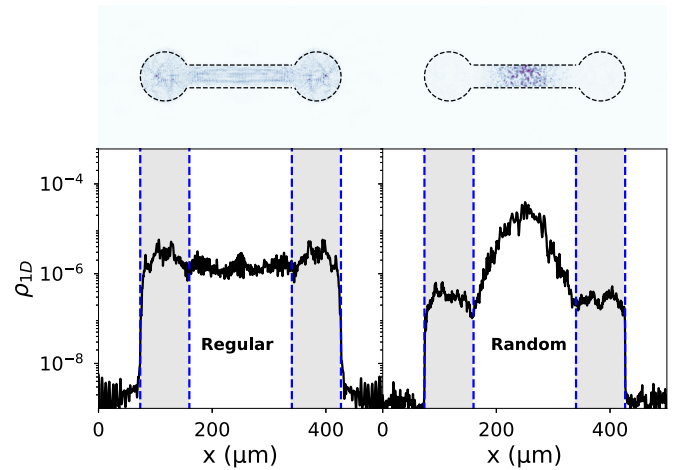


FIG. 11. A comparison of two-dimensional (top panels) and one-dimensional densities (bottom panels) after $t = 250$ ms time of expansion for impurities distributed regularly and randomly. The top panels provide a visual representation of ρ_{2D} within the dumbbell and suggest qualitatively different behavior for the two cases. In the case of regularly distributed impurities the density seems to be more or less uniform although it also shows weak filamentary structures, while the randomly distributed impurities seem to result in a more localized density distribution. The triangular shape of ρ_{1D} on the logarithmic scale is apparent for randomly distributed impurities, suggesting localization. The left and right reservoirs are indicated with shaded areas and vertical blue dashed lines.

Furthermore, we compare the momentum distributions for random and regular distributions in Fig. 13. Atoms are in the extended states in the regular case; therefore, the particles' distributions have a similar pattern in each segment. In contrast, particles just with high kinetic energy can reach to the left and right wells in the random case, since propagation of atoms halts due to Anderson localization. Therefore, there is a significant separation between the momentum distribution in three regions of the random case. The majority of particles within the channel have small $|k| < 1$, while those with

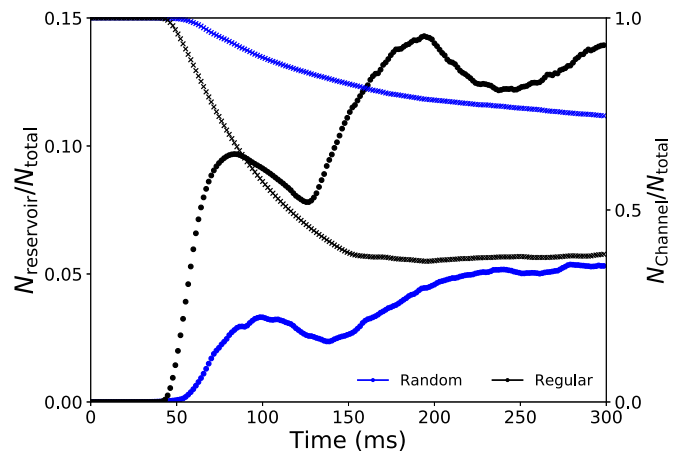


FIG. 12. Normalized number of particles in the channel (two curves starting on the top at $t = 0$) and in the reservoirs (two curves starting at the bottom at $t = 0$) are depicted as functions of time.

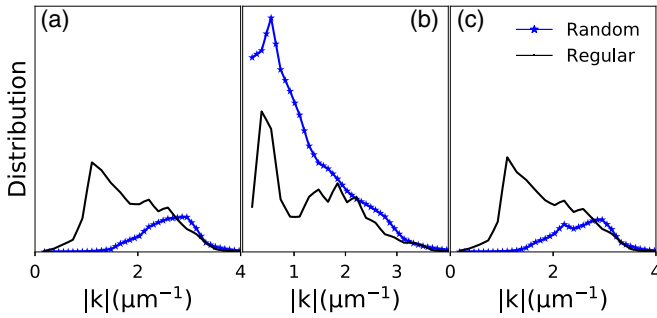


FIG. 13. Momentum distributions of atoms are shown in the three segments of the dumbbell for regularly and randomly distributed impurities at fill-factor $\eta = 0.2$. The left and right wells are depicted in panels (a) and (c), while panel (b) represents the channel segment. The black solid curves belong to the case of regularly distributed impurities, while the blue solid curves with star-shaped markers depict the data for the random distribution. The dumbbell geometry is given by $(L, W, R) = (180, 36, 45) \mu\text{m}$.

large $|k|$ could escape from the channel and move toward the wells.

C. Quantum impedance

As a final measure of the transport properties, we introduce a quantum analog of wave impedance, Z , which is usually interpreted as resistance experienced by a wave propagating in a medium (cf. electronics [53], acoustics [54], optics [55]). Quantum impedance was first defined by Brillouin [53] and later redefined by Khondker *et al.* [56] for a typical one-dimensional scatterer, i.e., a plane wave approaching a potential barrier of finite size with the wave reflected from and transmitted through this potential barrier. For the wave function ψ , the probability current density is $j = -i\frac{\hbar}{2m}[\psi^*(\nabla\psi) - \psi(\nabla\psi^*)]$. Introducing $\phi(x) = -i\frac{\hbar}{m}\nabla\psi$, one may also write $j \propto \text{Re}(\phi\psi^*)$, which resembles the expression for the average power, $\text{Re}(VI^*)$, delivered in an electrical circuit. The similarity suggests the introduction of a position-dependent quantum impedance:

$$Z(x) = \frac{\phi(x)}{\psi(x)}.$$

Specific cases, especially those considering periodic potential barriers within semiconductors, can be found in the literature [57–64]. Our focus here is mainly on suppressed matter wave transport. For localized states a significant part of the probability density is confined within a small volume (relative to the available volume) and hence must have exponential decay around the boundary of this small volume. We may thus assume that $\psi(x) \sim \psi_0(x)e^{-|x|/\xi}$, where ψ_0 is a slowly varying function and ξ is a characteristic length scale. With this assumption the impedance is real, and hence resistive, and $Z \sim (\nabla\psi_0/\psi_0) + 1/\xi$. Alternatively, for an extended state, $\psi(x) \sim \psi_0(x)e^{ikx}$, one would arrive at a complex impedance describing the interaction of a resistive element and a reactive element, and $Z \sim (\nabla\psi_0/\psi_0) + ik$.

We estimate $|Z|$ for a range of η for randomly and regularly distributed impurities. The results are shown in Fig. 14.

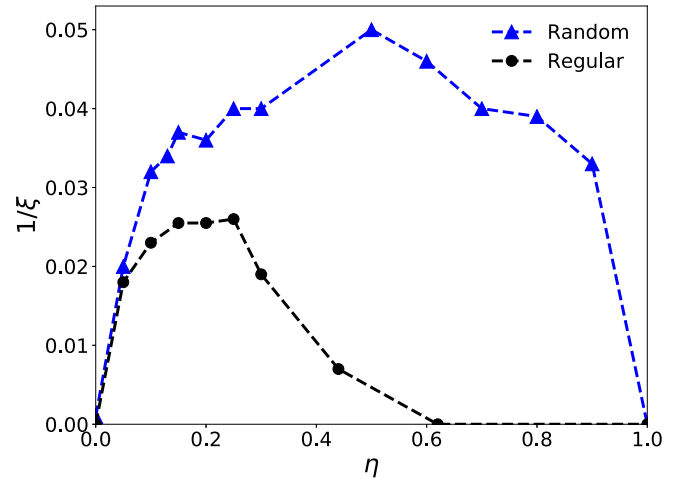


FIG. 14. The absolute value of impedance, $|Z|$, is plotted as a function of η for randomly (top curve) and regularly (bottom curve) distributed scatterers. The geometry is given by $(L, W, R) = (180, 36, 45) \mu\text{m}$.

As one can see for the random channel, $|Z|$ increases as a function of η and reaches its maximum for $\eta = 0.5$ before it decreases again and reaches its initial value. The scatterers are static. At $\eta = 0.5$, half of the channel is filled randomly by scatterers; however, for increasing η one may consider an elevated “bottom” potential which is decorated by holes with fill-factor $\eta_{\text{holes}} = 1 - \eta$. This particle-hole duality, used extensively in condensed matter physics, qualitatively explains the symmetry of Fig. 14. For regular distribution, however, $|Z|$ increases for $\eta \ll 1$, reaches a plateau lower than that for random disorder for $0.1 < \eta < 0.2$, and then rapidly diminishes for even higher fill-factors. This fast decay indicates the breakdown of our assumption for exponential decay of ψ , i.e., localization itself.

IV. CONCLUSION

We have studied propagation of a Bose-Einstein condensate in a 2D dumbbell-shaped trap with two realizations of impurities within the dumbbell channel. The dumbbell trap consists of two wells connected via a channel. The condensate is located initially in the middle of the channel and propagates through the channel towards the wells. We considered impurities within the channel of the dumbbell distributed first randomly and then regularly. The differences between the atomic transport through these channels was investigated and showed atoms stay in localized states in a randomly located disorder channel, while they are in extended states when impurities are placed periodically. We utilized the exponential decay profile of the 1D density of atoms to distinguish the localized regime from the nonlocalized regime. We also considered the momentum distributions of the atoms and showed particles with high energies can escape from being localized within the random disorder channel and reach the wells. These high-energy particles are in states with extension comparable to the system size and demonstrate an effective mobility edge due to the finite size of the system and the particular properties of our impurity potentials. We also defined and measured

an atomtronic impedance function $Z(\eta)$ for these two cases and showed a randomly located disorder channel has higher impedance in comparison with its regular counterpart.

Finally we mention two directions for future work. The first is investigating how Anderson localization depends on the regularity of the underlying disorder distribution or, in other words, the importance of how the correlation structure of

scatterers affect the onset of Anderson localization. A second avenue could be the analysis of the changes in the physical picture if thermal effects are also considered. We intuitively expect localization to prevail at sufficiently low, but nonzero temperatures, even though the thermalization process is not well understood [65–68]. A detailed study of these thermal effects could be of interest.

-
- [1] A. Haug, H. Massey, D. Haar, H. Massey, and H. Massey, *Theoretical Solid State Physics*, International Series of Monographs in the Science of the Solid State Vol. 1 (Pergamon, Elmsford, NY, 1972).
- [2] J. Sólyom, *Fundamentals of the Physics of Solids*, Vol. 1 (Springer-Verlag, Berlin, 2007).
- [3] A. Authier, *Early Days of X-Ray Crystallography* (Oxford University, Oxford, 2013).
- [4] P. A. Lee and T. V. Ramakrishnan, *Rev. Mod. Phys.* **57**, 287 (1985).
- [5] J. M. Ziman, *Models of Disorder* (Cambridge University, Cambridge, England, 1979).
- [6] N. Ashcroft and N. Mermin, *Solid State Physics* (Saunders, Philadelphia, 1976).
- [7] J. Ziman, *Electrons and Phonons: The Theory of Transport Phenomena in Solids*, International Series of Monographs on Physics (Clarendon, Oxford, 1960).
- [8] P. W. Anderson, *Phys. Rev.* **109**, 1492 (1958).
- [9] N. Mott and E. Davis, *Electronic Processes in Non-crystalline Materials* (Clarendon, Oxford, 1960).
- [10] N. F. Mott and W. Twose, *Adv. Phys.* **10**, 107 (1961).
- [11] P. Stollmann, *Caught by Disorder: Bound States in Random Media*, Progress in Mathematical Physics Vol. 20 (Springer Science & Business Media, Berlin, 2012).
- [12] D. Shechtman, I. Blech, D. Gratias, and J. W. Cahn, *Phys. Rev. Lett.* **53**, 1951 (1984).
- [13] J. B. Sokoloff, *Phys. Rev. Lett.* **58**, 2267 (1987).
- [14] J. B. Sokoloff, *Phys. Rev. B* **37**, 7091 (1988).
- [15] Y. Jian, *Z. Phys. B* **88**, 141 (1992).
- [16] E. Abrahams, P. W. Anderson, D. C. Licciardello, and T. V. Ramakrishnan, *Phys. Rev. Lett.* **42**, 673 (1979).
- [17] E. Abrahams, *50 Years of Anderson Localization* (World Scientific, Singapore, 2010).
- [18] M. Cutler and N. F. Mott, *Phys. Rev.* **181**, 1336 (1969).
- [19] R. L. Weaver, *Wave Motion* **12**, 129 (1990).
- [20] R. Dalichaouch, J. P. Armstrong, S. Schultz, P. M. Platzman, and S. L. McCall, *Nature (London)* **354**, 53 (1991).
- [21] D. S. Wiersma, P. Bartolini, A. Lagendijk, and R. Righini, *Nature (London)* **390**, 671 (1997).
- [22] M. Stoytchev and A. Z. Genack, *Phys. Rev. B* **55**, R8617 (1997).
- [23] C. Dembowski, H.-D. Gräf, R. Hofferbert, H. Rehfeld, A. Richter, and T. Weiland, *Phys. Rev. E* **60**, 3942 (1999).
- [24] M. Störzer, P. Gross, C. M. Aegerter, and G. Maret, *Phys. Rev. Lett.* **96**, 063904 (2006).
- [25] D. Laurent, O. Legrand, P. Sebbah, C. Vanneste, and F. Mortessagne, *Phys. Rev. Lett.* **99**, 253902 (2007).
- [26] T. Schwartz, G. Bartal, S. Fishman, and M. Segev, *Nature (London)* **446**, 52 (2007).
- [27] H. Hu, A. Strybulevych, J. H. Page, S. E. Skipetrov, and B. A. van Tiggelen, *Nat. Phys.* **4**, 945 (2008).
- [28] J. Chabé, G. Lemarié, B. Grémaud, D. Delande, P. Szriftgiser, and J. C. Garreau, *Phys. Rev. Lett.* **101**, 255702 (2008).
- [29] F. Riboli, P. Barthelemy, S. Vignolini, F. Intonti, A. D. Rossi, S. Combrie, and D. S. Wiersma, *Opt. Lett.* **36**, 127 (2011).
- [30] T. Sperling, W. Bührer, C. M. Aegerter, and G. Maret, *Nat. Photonics* **7**, 48 (2012).
- [31] M. Lopez, J.-F. Clément, P. Szriftgiser, J. C. Garreau, and D. Delande, *Phys. Rev. Lett.* **108**, 095701 (2012).
- [32] I. Manai, J.-F. Clément, R. Chicireanu, C. Hainaut, J. C. Garreau, P. Szriftgiser, and D. Delande, *Phys. Rev. Lett.* **115**, 240603 (2015).
- [33] T. Ying, Y. Gu, X. Chen, X. Wang, S. Jin, L. Zhao, W. Zhang, and X. Chen, *Sci. Adv.* **2**, e1501283 (2016).
- [34] S. Fishman, Y. Krivolapov, and A. Soffer, *Nonlinearity* **25**, R53 (2012).
- [35] D. L. Shepelyansky, *Phys. Rev. Lett.* **70**, 1787 (1993).
- [36] B. Shapiro, *J. Phys. A: Math. Theor.* **45**, 143001 (2012).
- [37] G. Bergmann, *Phys. Rep.* **107**, 1 (1984).
- [38] G. Bergmann, *Phys. Rev. Lett.* **48**, 1046 (1982).
- [39] S. S. Kondov, W. R. McGehee, J. J. Zirbel, and B. DeMarco, *Science* **334**, 66 (2011).
- [40] J. Billy, V. Josse, Z. Zuo, A. Bernard, B. Hambrecht, P. Lugan, D. Clément, L. Sanchez-Palencia, P. Bouyer, and A. Aspect, *Nature (London)* **453**, 891 (2008).
- [41] G. Roati, C. D’Errico, L. Fallani, M. Fattori, C. Fort, M. Zaccanti, G. Modugno, M. Modugno, and M. Inguscio, *Nature (London)* **453**, 895 (2008).
- [42] F. Jendrzejewski, A. Bernard, K. Müller, P. Cheinet, V. Josse, M. Piraud, L. Pezzé, L. Sanchez-Palencia, A. Aspect, and P. Bouyer, *Nat. Phys.* **8**, 398 (2011).
- [43] F. N. Mott, M. Pepper, S. Pollitt, R. H. Wallis, and C. J. Adkins, *Proc. R. Soc. Lond. A. Math. Phys. Sci.* **345**, 169 (1975).
- [44] D. H. White, T. A. Haase, D. J. Brown, M. D. Hoogerland, M. S. Najafabadi, J. L. Helm, C. Gies, D. Schumayer, and D. A. Hutchinson, *Nat. Commun.* **11**, 4942 (2020).
- [45] M. Robert-de-Saint-Vincent, J.-P. Brantut, B. Allard, T. Plisson, L. Pezzé, L. Sanchez-Palencia, A. Aspect, T. Bourdel, and P. Bouyer, *Phys. Rev. Lett.* **104**, 220602 (2010).
- [46] F. Jendrzejewski, K. Müller, J. Richard, A. Date, T. Plisson, P. Bouyer, A. Aspect, and V. Josse, *Phys. Rev. Lett.* **109**, 195302 (2012).
- [47] J. Huntley, *Appl. Opt.* **28**, 4316 (1989).
- [48] S. Pilati, S. Giorgini, M. Modugno, and N. Prokof’ev, *New J. Phys.* **12**, 073003 (2010).
- [49] W. Morong and B. DeMarco, *Phys. Rev. A* **92**, 023625 (2015).
- [50] R. Kosloff and H. Tal-Ezer, *Chem. Phys. Lett.* **127**, 223 (1986).

- [51] W. H. Press, S. A. Teukolsky, B. P. Flannery, and W. T. Vetterling, *Numerical Recipes in Fortran 77: The Art of Scientific Computing (Vol. 1 of Fortran Numerical Recipes)* (Cambridge University Press, 1997).
- [52] The goodness-of-fit R_{fit}^2 varies in [0,1] and indicates the quality of the fit.
- [53] L. Brillouin, *Wave Propagation in Periodic Structures: Electric Filters and Crystal Lattices* (Dover Publications, Mineola, 2003).
- [54] I. Dunn and W. Davern, *Appl. Acoustics* **19**, 321 (1986).
- [55] R. Kronig, B. Blaisse, and J. J. V. D. Sande, *App. Sci. Res., Sect. B* **1**, 63 (1950).
- [56] A. N. Khondker, M. R. Khan, and A. F. M. Anwar, *J. Appl. Phys.* **63**, 5191 (1988).
- [57] S. M. F. Kabir, M. R. Khan, and M. A. Alam, *Solid-State Electron.* **34**, 1466 (1991).
- [58] N. Ohtani, N. Nagai, M. Suzuki, and N. Miki, *Electron. Commun. Jpn. (Part II: Electronics)* **74**, 11 (1991).
- [59] D. J. Griffiths and N. F. Taussig, *Am. J. Phys.* **60**, 883 (1992).
- [60] H. Sanada, N. Nagai, N. Ohtani, N. Miki, and H. Ohkama, *Electron. Commun. Jpn. (Part II: Electronics)* **77**, 15 (1994).
- [61] H. Sanada, N. Nagai, N. Ohtani, and N. Miki, *Electron. Commun. Jpn. (Part II: Electronics)* **77**, 106 (1994).
- [62] H. Sanada, J. Ren, and N. Nagai, *Electron. Commun. Jpn. (Part II: Electronics)* **78**, 39 (1995).
- [63] E. A. Nelin, *Phys.-Usp.* **50**, 293 (2007).
- [64] B. Gutiérrez-Medina, *Am. J. Phys.* **81**, 104 (2013).
- [65] C. Connaughton, C. Josserand, A. Picozzi, Y. Pomeau, and S. Rica, *Phys. Rev. Lett.* **95**, 263901 (2005).
- [66] N. Cherroret, T. Karpiuk, B. Grémaud, and C. Miniatura, *Phys. Rev. A* **92**, 063614 (2015).
- [67] C.-H. Hsueh, M. Tsubota, and W.-C. Wu, *J. Low Temp. Phys.* **196**, 13 (2019).
- [68] T. Scoquart, T. Wellens, D. Delande, and N. Cherroret, *Phys. Rev. Research* **2**, 033349 (2020).